

Visualization of Blood Vessels in *in-vitro* Raw Speckle Images Using an Energy-based on DWT Coefficients

Francisco Javier Lopez-Tiro^a, Hayde Peregrina-Barreto^a, Jose de Jesus Rangel-Magdaleno^{a,*}, Julio Cesar Ramirez-San-Juan^a

^a*Instituto Nacional de Astrofisica, Optica y Electronica, Luis Enrique Erro 1, Santa Maria Tonantzintla, Puebla, Mexico*

Abstract

The visualization and localization of blood vessels is an important task to determine the presence and the health status of microvasculature in the biological tissue. Laser Speckle Contrast Imaging is one of the most widely employed techniques to study blood vessels; even so, it has some drawbacks in analyzing deep blood vessels ($> 100\mu m$) since the image noise level increases.

The Wavelet Approach is a model of automatic denoising for contrasted *in-vitro* Raw Speckle images using an energy criterion. The criterion selects the more suitable denoising level from the Discrete Wavelet Transform decomposition using the detail coefficients. Then, the segmentation of low-noise images by mathematical morphology techniques establish the blood vessel and biological tissue location. Finally, the region corresponding to the blood vessel and the low-noise images are used to improve the visualization of blood vessels.

Results show that a Wavelet Approach improves the visualization of blood vessels up to a depth of $400\mu m$. Furthermore, the proposed model demonstrates that the automatic denoising criterion improves the localization of superficial ($\leq 100\mu m$) and deep ($> 100\mu m$) blood vessels.

Keywords: Visualization of blood vessels, Laser Speckle Contrast Imaging, Raw Speckle Image, Wavelet approach, Discrete Wavelet Transform.

*Corresponding author

Email address: jrangel@inaoep.mx (Jose de Jesus Rangel-Magdaleno)
URL: <https://www.inaoep.mx/> (Jose de Jesus Rangel-Magdaleno)

1. Introduction

Visualization of blood vessels (VBV) is an important task for a wide variety of biomedical applications, such as neuroscience [1], dermatology [2], and ophthalmology [3]. Laser Speckle Contrast Imaging (LSCI) is the most used 5 technique for improving VBV from a Raw Speckle Image (RSI). LSCI uses contrast values as a new representation of the RSIs to improve VBV. LSCI systems have some limitations due to the strong scattering of static structures (such as skull or epidermis) that make difficult the visualization of blood vessels (BV) inside the biological tissue (BT) [4]. One of these limitations is the loss of contrast 10 between the BT and the BV as depth increases [5] which reduces the VBV.

To improve the VBV, different strategies based on physical, instrumental, and computational methods have been implemented. Physical improvements performed during the RSIs acquisition have reported significant results [6, 7, 8]. However, these techniques become invasive since they involve external agents 15 in the skin or introduce foreign particles to the blood flow, which could not be adequate in sensitive regions such as the retina or brain. The instrumental improvements before and during the acquisition of RSIs are non-invasive techniques for calculating and correcting the effect of scattering with a single exposure time [9]. However, these techniques are limited when the level of scattering 20 in the sample is high, and a long exposure time can cause heating or burns to the BT. Several methods have proposed approaches to compute contrast values from RSIs. In Ref. [4], it was performed an extensive review of state of the art on traditional contrast methods that use isotropic analysis windows including *in-vitro*, *in-vivo*, and *ex-vivo* applications. Traditional contrast methods comprise 25 the spatial (sK), temporal (tK), and spatiotemporal (stK) approaches. Other non-traditional contrast methods use anisotropic analysis windows [10, 11, 12], or a combination of traditional methods of contrast [13, 14]. Although a contrast representation is helpful in the VBV, its quality is affected by a noise increment when the depth of the BV is high ($> 100\mu m$) in traditional and non-traditional

30 contrast methods. Some works have focused on improve the VBV [15, 16, 17],
localization of blood vessels (LBV)[18, 19], or both [20, 21, 22] at low and high
depths ($0\mu m - 900\mu m$). Contrast improvement models have been developed.
These models allow to improve the VBV [15, 16, 17] or localization of blood
vessels (LBV) [18, 19] (in some cases both [20, 21, 22]) of BV at low and high
35 depths ($0\mu m - 900\mu m$). An alternative approach to estimate the blood flow
speed is the speckle correlation, in fact, it is well known that the speckle corre-
lation is close related with the speed of the blood flow for superficial and deep
BV as shown in [23, 24, 25].

In this work, we propose a methodology to improve the VBV from *in-vitro*
40 RSIs based on the analysis of the Discrete Wavelet Transform (DWT). The
main contribution of this work is the automatic selection of a decomposition
level during the DWT denoising process, which is a common problem in DWT
denoising methods [19, 26]. Obtained results have demonstrated that the use
of an automatic denoising criterion attenuates the noise level in the BV region
45 and improves the VBV in superficial and deep *in-vitro* RSIs.

2. Methods

The Wavelet Approach (WA) methodology performs four steps: i) contrast
calculation of the RSI packages, ii) denoising through automatic filtering crite-
ria, iii) contrast values classification into BV and BT through a segmentation
50 method, and iv) an assembly of the denoising contrast values and the classes
obtained from the segmentation. Fig. 1 shows a framework of the proposed
methodology.

2.1. Data

The experimental setup consists of a He-Ne laser ($632.8nm$) that homoge-
55 neously illuminates a skin phantom using an optical diffuser (Model ED1-C20,
Thorlabs Inc). A set of RSIs was acquired by a CCD camera (Model Retiga
2000R, QImaging, Canada) equipped with a macro lens. The skin phantoms

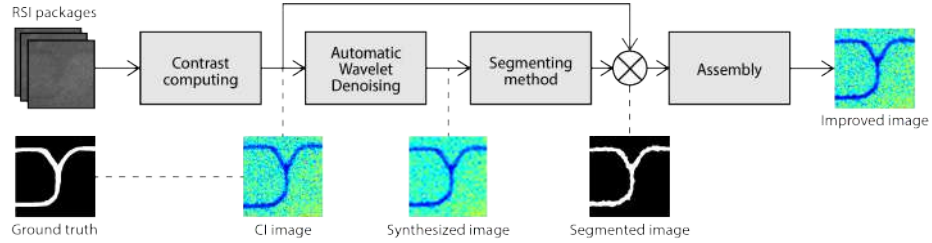


Figure 1: Framework of the proposed wavelet approach.

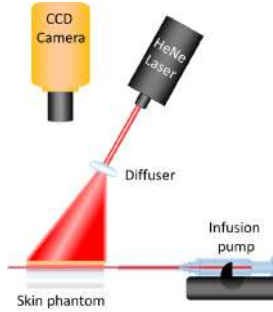


Figure 2: Experimental setup employed to acquire RSIs sets from straight and bifurcated BVs.

were manufactured with optical properties (scattering coefficient) similar to human skin, as reported in [27]. Two phantoms were used: one for the epidermis and one for the dermis. Different epidermis layer thicknesses that go from $0\mu m$ to $900\mu m$ were used to vary each $100\mu m$ the depth (ρ) of BV. BV in the skin phantom was simulated through two configurations: a straight glass capillary with an inside diameter of $700\mu m$ and a bifurcated microchannel with an inside diameter of $700\mu m$ (thinXXS Microtechnology AG, Germany). In both configurations, the BV was located on the surface of the dermis. The infusion of intralipid at 3% in water was used to simulate the scattering properties of human blood and was pumped through the capillaries with a pump (Model NE-500, NewEraPumpSystemInc). The speed of flow in the BV is denoted as v . Two values for v were used: $5mm/s$ for straight BV and $20mm/s$ for bifurcated BV. A similar range of speeds has been used in similar experiments [28, 29, 30]. The dimensions of the RSIs are 344×329 pixels and 280×288 pixels to straight

and bifurcated BV, respectively. The specifications of the RSI set are described in Table 1.

Table 1: Specifications of *in-vitro* RSI set.

BV	Depth μm	Dimensions $pixels$	Blood flow speed mm/s
Straight	0, 200, 400, 500, 600, 700, 900	344×329	5
Bifurcated	200, 300, 400, 500, 600, 700, 900	280×288	20

Through the experimental setup (Fig. 2), 14 sets of *in-vitro* RSIs were acquired, where each set contains 30 RSI from superficial and deep BVs.
75

2.2. Contrast

Contrast (K) is the most widely used method to improve the VBV of RSIs, and is defined as the cocient between the standard deviation ($\sigma(W)$) and the average intensity ($\bar{I}(W)$) (1).

$$K(x, y) = \frac{\sigma(W)}{\bar{I}(W)} \quad (1)$$

80 Where (W) is an analysis window that moves through the RSI [4]. By definition, contrast values are normalized between 0 and 1. Values close to 0 indicate a low contrast and are related to the BV (low contrast value variation). On the other hand, values close to 1 indicate high contrast and are related to the BT [5]. The most commonly used method for contrast calculation is the spatial contrast (sK), which employs a square sliding analysis window $W_{d \times d}^{sK}$, where d is the size of the window. A variant of sK is the spatial contrast averaged (s $Kavg$), it calculates the average of a set of f sK images Eq. (2). $sKavg$ improves the spatial resolution of the contrast image (CI) at the cost of the temporal resolution.
85

$$sKavg(x, y) = \frac{1}{f} \sum_{i=1}^f sK(x, y) \quad (2)$$

90 Figure 3 shows the CIs employed to calculate $sKavg$ ($f = 30$) by using an analysis window $d = 5$. In CIs, at low depths, close to $0\mu m$, it is easy to distinguish the localization of the BV. However, at high depths, close to $900\mu m$, it is not easy to determine the boundaries between BV and BT.

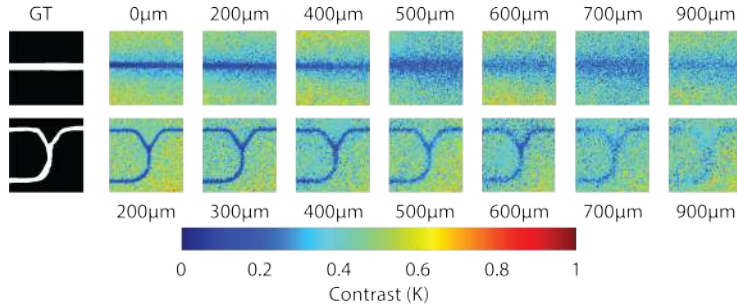


Figure 3: Effect of the depth of the BV inside BT for the CI set. VBV at low depths (close to $0\mu m$) is good, however it declines as depth increases.

95 One feature of CIs is the histogram distribution (HD) of contrast values. On the one hand, when the depth of the BV inside the BT is low ($\rho < 100\mu m$), the HD of the CI is bimodal, where it is easy to establish a value that separates two regions (BV and BT). On the other hand, when the depth of BV inside the BT increases ($\rho > 100\mu m$), the HD is unimodal, in which it is difficult to identify two regions. As can be seen, it is desired to avoid a unimodal HD. Therefore, a
100 method is needed to convert contrast values from unimodal HD to bimodal HD without losing spatial resolution.

2.3. Denoising

105 Due to the noisy nature of CIs, they require filtering or denoising methods to improve the VBV. In deep BV, filtering methods in CIs are efficient at attenuating noise. However, they have the disadvantage of fusing the information between the regions (BV and BT), affecting the VBV.

In related work, [16, 20, 22] establishes denoising models as an alternative when there are fusion problems. In the work [22] they present the PCA model and select the first principal components and return an image without fusion

110 effects. However, the noise attenuation is not entirely efficient, affecting the VBV and LBV. In the works [16, 20], they introduce the use of the Wavelet Transform in CIs as a solution to noise and fusion problems. Wavelet domain has been successfully proven in noise attenuation, as it provides better spatial and spectral resolution in images than other techniques such as Fourier Transform (FT) [31, 32, 33]. DWT can be interpreted as a process of decomposition and reconstruction for multiple levels of filtering (Fig. 4).

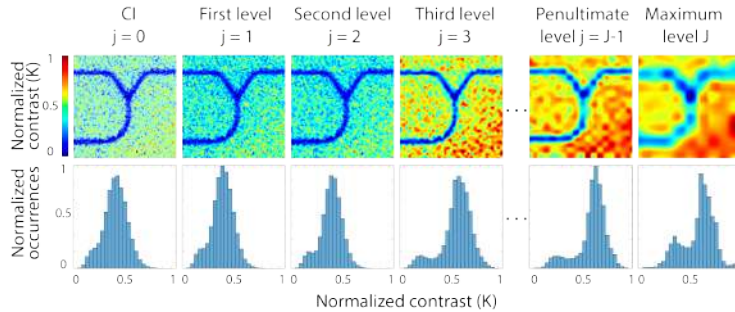


Figure 4: Process of decomposition and reconstruction of J -levels in CI of a bifurcated BV at $300\mu m$ depth (top row), and their corresponding HD for each j -level (bottom row).

A filtering level (j) can take multiple integer values such as $1 \leq j \leq J$, where (J) is the maximum filtering level. An important feature is that at each filtering level, the noise in the image decays by 2^j . Although DWT is an efficient 120 method of noise attenuation, the incorrect choice of j -level in the decomposition process can cause fusion problems (we are trying to avoid it). Therefore, a method is needed to calculate the j level automatically. The solution is to set an automatic denoising criterion on the approximation or detail coefficients of CIs, independent of the depth of the BV.

125 2.3.1. Decomposition

DWT decomposition process (DWT-DP) filters spatial information from a CI ($K(x, y)$) of $M \times N$ pixels, through the high-pass ($\bar{h}[k]$) and low-pass ($\bar{g}[k]$) filters defined by a wavelet function (where $[k]$ is the number of coefficients that describe the filter [34]). Wavelet functions (ψ) are generated by dilation and

130 translation operations, starting from a single function called mother wavelet [35]. The choice of the wavelet function gives rise to different multiresolution analyses. However, the most useful scaling functions are those with compact support such as the Daubechies mother wavelet (for details, see [36]).

135 After filtering, it goes through a sub-sampling process $\downarrow 2$, where the CI dimensions are reduced by a scale of 2^j in the x direction of the CI. Then, the same process is repeated in the y direction of the CI. The result of the DWT-DP (Fig. 5) are the approximation and detail coefficients (AC and DC, respectively) at j -level with dimensions $M/2^j \times N/2^j$. On the one hand, AC denoted as LL_j represents a low-frequency image. On the other hand, the horizontal (LH_j),
140 vertical (HL_j), and diagonal (HH_j) DC, are the noise in different directions of the CI.

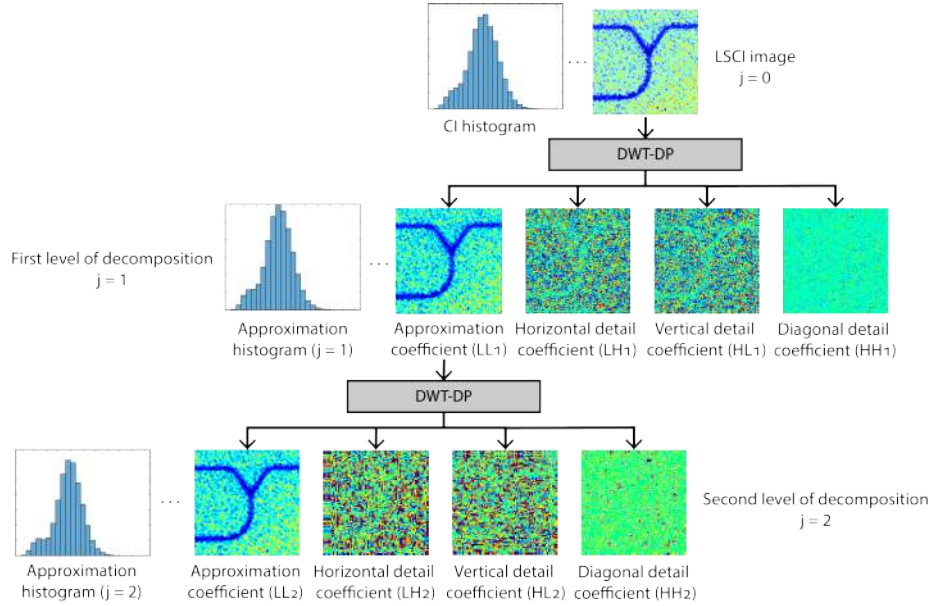


Figure 5: DWT-DP for levels $j = 1$ and $j = 2$, in CI of a bifurcated BV at $300\mu\text{m}$ depth. For each j -level, the approximation (LL_j) and detail (LH_j , HL_j , and HH_j) coefficients are obtained. In LSCI applications, the DWT-DP is done in the AC (LL_j) that maintain the relevant information of the BV.

A common problem in the DWT-DP is the choice of parameters j -level and

ψ . An incorrect selection of them (in a noisy image as CI, $\rho > 100\mu m$) could cause two unwanted events. First, preserve a high amount of noise in the AC (producing a unimodal HD). Second, it can fuse information from the AC and DC (over filtering). To solve this problem, J is established as a way to avoid over filtering. However, J is not always the optimal level of filtering, as it could merge information from AC and DC during the DWT-DP. Different criteria have been established to select the optimal filtering level (J^*) [37, 38, 39]. The automatic denoising criterion selects the best j -level among J (during the DWT-DP). To find J^* in a CI, a study of AC and DC energy is established for each of the levels $j = \{1, 2, \dots, J\}$ [39]. The energy of each approximation coefficient is calculated as the energy of the ACs of J :

$$E_A^J = \sum_x \sum_y (K_{LL,J}(x, y))^2 \quad (3a)$$

The energy of DC of j -level are given by:

$$E_\beta^j = \sum_x \sum_y (K_\beta(x, y))^2, \quad j = 1, 2, \dots, J \quad (3b)$$

$\beta = (LH_j, HL_j, HH_j)$ corresponds to the vertical, horizontal and diagonal DC, respectively. The total energy of CI $K(x, y)$ at the J -level is given as $E = E_A^J + \sum_\beta E_\beta^j$.

The normalized energy of each coefficient is defined as:

$$E_A = \frac{E_A^J}{E} \quad (4a)$$

$$E_D = \sum_\beta \left(\frac{1}{E} \sum_{j=1}^J E_\beta^j \right) \quad (4b)$$

E_A is the normalized energy of the AC, and E_D is the normalized energy of the DC. The normalized energy E_A is significantly higher than that of the DC. The choice of j -level is based on the energy ratio of the DC of two

consecutive levels. Let D_j be the sum of normalized energies of the three detail coefficients of the j -level:

$$D_j = \frac{\sum_{\beta} E_{\beta}^j}{E} \quad (5)$$

R_j is the energy relation of the DC between levels:

$$R_j = \frac{D_j}{D_{j-1}}, \quad j = 1, 2, \dots, J \quad (6)$$

J^* is selected when R_j is a minimum:

$$J^* = \min(R_j) \quad (7)$$

The minimum value of R_j represents that the energy in the DC between two consecutive levels are sufficiently separated in terms of marginal improvement and that the DWT-DP must be stopped. For the $j < J^*$, R_j indicates that the amount of energy in DC is low and that there is noise in AC that requires an additional filtering level. For the filtering level $j > J^*$, R_j indicates that the amount of energy in the DC is high and that an overflow of energy in DC exists and implies a fusion of information from the coefficients during the reconstruction process.

2.3.2. Reconstruction

The DWT reconstruction process (DWT-RP) is the reverse of the DWT-DP. In DWT-RP given a filtering level $j \geq 1$, it allows to assemble the information of the coefficients (LL_j , HL_j , LH_j , HH_j) through the processes of oversampling $[\uparrow 2]$ and filtering through the reconstruction filters ($\tilde{g}[k]$ and $\tilde{h}[k]$). In LSCI applications, DWT-RP is performed with AC information (LL_j) of size $M/2^j \times N/2^j$. The DC coefficients are not used to reconstruct the image since it is not desired to recover the noise separated during DWT-DP. Then, the DC coefficients were processed as empty elements. DWT-RP allows to attenuate the noise of the DC and retrieve a synthesized image ($\dot{K}(x, y)$) of dimensions $M \times N$.

In the presented methodology, $j = J^*$ is selected using an automatic denoising criterion based on the energy of the DC in multiple levels. The maximum level of filtering selected was $J = 5$. Levels greater than 5 were discarded due to the number of coefficients of ψ , which limits the number of j -levels in the CIs (of dimensions of $M \times N$). The wavelet function (ψ) selected was *Daubechies 5* as it implies a low computational cost.

190 2.4. Segmentation

Under the assumption that the contrast values in the synthesized image ($\dot{K}(x, y)$) have a bimodal HD, due to attenuated noise after the DWT-DP and DWT-RP, the regions of interest (BV and BT) can be separated with a thresholding process and segmented with a morphological processing.

195 2.4.1. Thresholding

Consider the HD (Fig. 6e) of a synthesized image ($\dot{K}(x, y)$) of a bifurcated BV (Fig. 6b). The HD of the synthesized image can be described as two peaks separated by a valley. On the one hand, the small peak on the left side represents the BV information because this region keeps low contrast values (Fig. 6b). On the other hand, the prominent peak on the right side corresponds to the BT information with high contrast values (C_2). Finally, the valley in the central region is a transition zone between the BV and BT (C_3). Given the above, it is possible to establish three classes: BV, transition zone, and BT, denoted as C_1 , C_2 and C_3 , respectively. A simple way to classify each pixel in the synthesized image ($\dot{K}(x, y)$) is through a thresholding process for multiple classes [40]:

$$Q(x, y) = \begin{cases} C_1, & \text{if } 0 \leq \dot{K}(x, y) < T_1 \\ C_2, & \text{if } T_1 \leq \dot{K}(x, y) < T_2 \\ C_3, & \text{if } T_2 \leq \dot{K}(x, y) < L \end{cases} \quad (8)$$

Where, C_1 , C_2 , and C_3 are the classes of the quantized image ($Q(x, y)$) in which each pixel of the synthesized image ($\dot{K}(x, y)$) can be classified. L is the

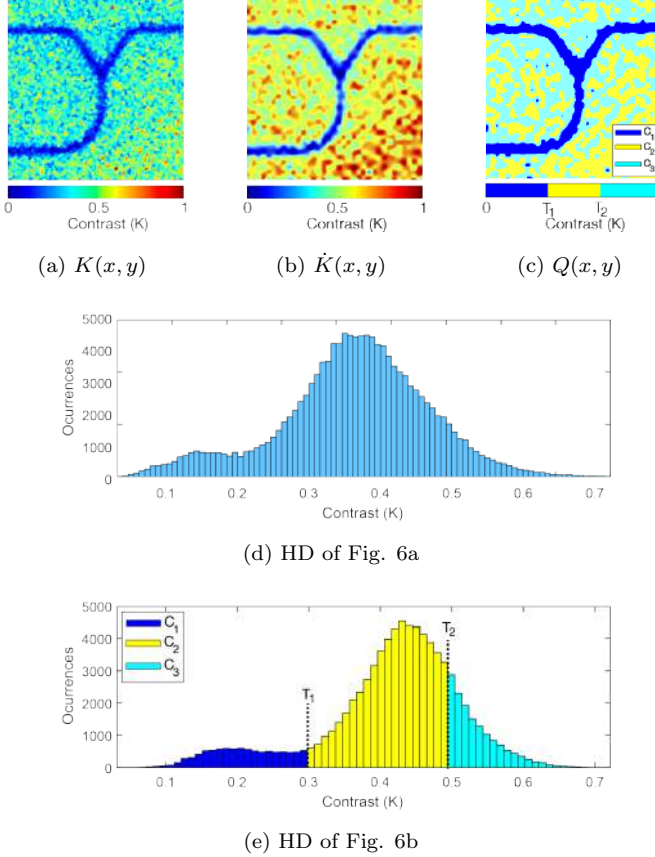


Figure 6: (a) Contrast image ($K(x, y)$) at $j = 0$ of a bifurcated BV at $300\mu m$ depth, and their (b) synthesized image ($\dot{K}(x, y)$). (c) Quantized image ($Q(x, y)$) of (b). (d) HD of the contrast image and (e) HD of the synthesized image indicating the classes (C_1 , C_2 and C_3) and their threshold values (T_1 and T_2).

maximum contrast value of the synthesized image. Also, T_1 and T_2 represent the
 210 threshold values. The threshold value T_1 is the limit between classes C_1 and C_2 , while the threshold value T_2 is the limit between classes C_2 and C_3 . The main problem in the thresholding process is to select the values of T that correctly identify the classes. To solve this problem, the Otsu method is implemented [41], which automatically estimates the T threshold values by analyzing the
 215 individual image distribution.

The result of the thresholding process is a quantized image ($Q(x, y)$) (Fig. 6c). Subsequently, to construct a binarized image ($B(x, y)$) from the quantized image, the classes C_2 and C_3 were joined in a single class C_{2-3} due to the similarity between them and their close association to the BT (for details, see [26]), reducing the number of classes from three to two (C_1, C_{2-3}) and the number of thresholds from two to one (T_1). The result of threshold processing is a binarized image ($B(x, y)$), with two classes, the BV is denoted as 1, while the BT and the transition zone is 0.

2.4.2. Morphological processing

After the thresholding process, there are usually small isolated particles and rough edges around the BV in the binarized image ($B(x, y)$), which increases the rate of false positives. To avoid this effect, an area criterion (α) is used to eliminate particles that are not of interest. The connected objects that meet criterion α are kept; otherwise, the object is deleted. In this work $\alpha = 200$ connected pixels of C_1 . Rough edges are attenuated with a morphological closing operation ($B \circ \lambda$) defined as a dilation followed by erosion:

$$B \circ \lambda = (B \oplus \lambda) \ominus \lambda \quad (9)$$

where a binarized image ($B(x, y)$) is operated by a structural element (λ), the size of λ is in the order of the elements surrounding the BV. In this work, a structural element was selected with a radius of seven pixels. When applying the morphological closing operation, the elements that the area criterion did not manage to eliminate are removed. Consequently, it reduces the roughness of the BV region. The result of the morphological processing is a segmented image ($S(x, y)$) of two classes (Fig. 7b), where the BV is denoted as 1, while the BT is 0. An objective way to establish the results of the LBV is through a similarity metric between segmented image ($S(x, y)$) and GT. In this work, the evaluation metrics accuracy, precision, similarity, sensibility, and Jaccard index (JI) were used.

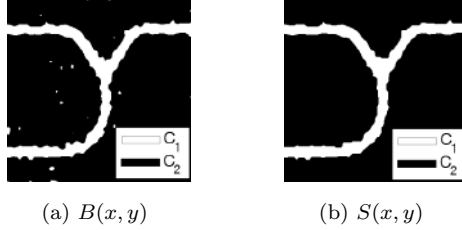


Figure 7: Segmentation process of (a) binarized image ($B(x, y)$) with morphological processing. As a result, (b) a segmented image ($S(x, y)$) is obtained (after applying an area criterion and operating with morphological closing).

2.5. Visualization improvement

Commonly, traditional methods of contrast are limited to increase the VBV through some filtering techniques. However, in Ref. [15, 21], it has been demonstrated that the LBV can be useful to improve the contrast values in specific regions such as the BV. In this work, the segmentation process of the BV and the BT from the synthesized image ($\dot{K}(x, y)$) is carried out.

The WA model proposes an assembly defined by (10), that is, for each pixel that corresponds to the BV in the segmented image ($S(x, y)$), the contrast value of the synthesized image ($\dot{K}(x, y)$) is assigned in the improved image ($W(x, y)$). On the other hand, for each pixel that corresponds to the BT in the segmented image ($S(x, y)$), the contrast value of the CI ($K(x, y)$) is assigned in the improved image ($W(x, y)$).

$$W(x, y) = \begin{cases} \dot{K}(x, y), & \text{if } S(x, y) = 1 \\ K(x, y), & \text{if } S(x, y) = 0 \end{cases} \quad (10)$$

In Fig. 8a, it is observed that contrast values corresponding to the BV maintain a high amount of noise (a mixture of high and low-frequency information) compared to the blood vessel region in the improved image ($W(x, y)$). This effect is evident when the depth of the BV increases, making it difficult to distinguish between the two regions. When depth and noise are high ($\rho \approx 900\mu m$), the contrast values are similar at both edges and in the center of the BV. Conse-

quently, VBV will be affected, and it may be challenging to appreciate contrast values in the central region of the BV. The improved image ($W(x, y)$) shows a low-frequency representation of the contrast values along with the BV, where it can be observed that the contrast values are more homogeneous with low noise in the BV. The improved image (Fig. 8b) allows to visualize along the BV that contrast values increase when closer to the edge, and contrast values decrease when closer to the central region of BV.

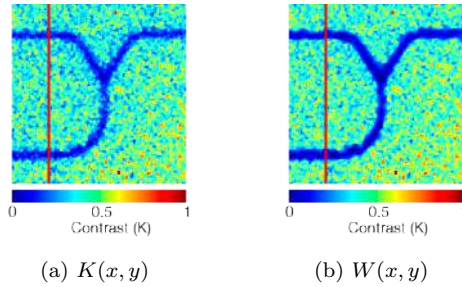


Figure 8: (a) CI ($K(x, y)$) of a bifurcated BV at $300\mu\text{m}$ depth. (b) Improved image ($W(x, y)$) with the proposed WA methodology.

For subjective evaluation of the proposed WA model, a contrast profile analysis was performed. Two contrast profiles (Fig. 9a) were taken from a sample column of a superficial bifurcated BV (red lines in Fig. 8). The $sKavg$ contrast is denoted as a black profile, while a red profile is associated with WA.

Two contrast profiles (Fig. 9a) were taken from a sample column of a superficial bifurcated BV (red lines in Fig. 8). The $sKavg$ contrast is denoted as a black profile, while a red profile is associated with WA. The contrast profiles have two downwardly oriented peaks corresponding to the region of the BV. The peaks are around samples 50 and 245 (Fig. 9b and Fig. 9c, respectively). On the one hand, in the $sKavg$ contrast profile, it can be seen that the contrast values follow a behavior with rapid changes. This behavior is related to the noise inside the BV. On the other hand, in the WA contrast profile, the contrast values have a softening behavior. Besides, it is possible to determine the center of the BV as a local minimum.

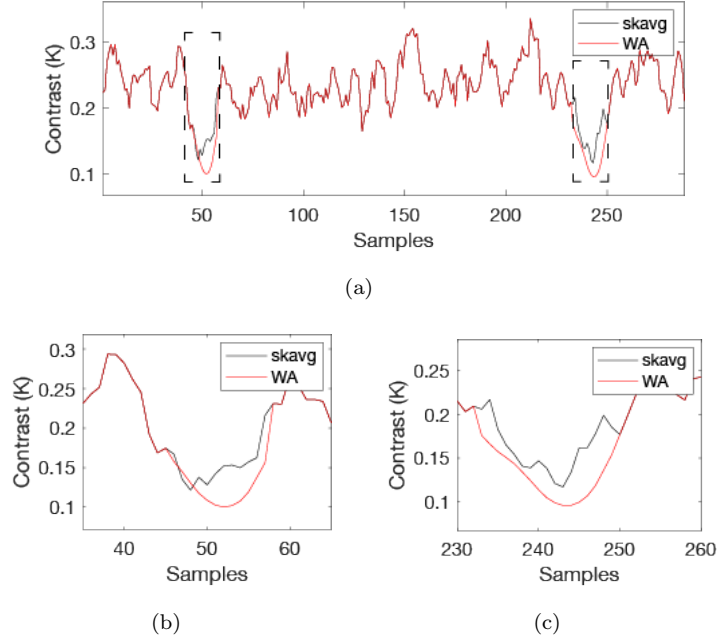


Figure 9: (a) Contrast profile along column 50, (b) and (c) contrast profiles of two downwardly oriented peaks corresponding to the region of the BV.

An objective way to establish the results of VBV is through an image quality metric between segmented image ($S(x, y)$) and improved image ($W(x, y)$). In this work, Contrast-to-Noise Ratio (CNR) and kurtosis (κ) were used as evaluation metrics.
285

3. Results

3.1. Automatic denoising criterion

A common problem in LBV models with the DWT is the selection of j -level. The selection of the j -level allows to filter a CI and obtain a synthesized image.
290 The synthesized image allows having a binarized image that can be compared with the GT. As described in the Sec. 2.3.1, an incorrect selection of the j -level may imply some drawbacks, for example, over-segmentation of the BV when the j -level is high or keeping a high amount of noise in the synthesized image when the j -level is low.

295 One way to select j -level is to evaluate the performance of LBV with some
metrics. The JI metric was used to measure the performance between the LBV
of the proposed WA model and the GT of the RSI set. In the Table 2 are shown
the LBV results of the proposed WA model for $j = \{1 \dots J\}$. The maximum
filtering level selected was $J = 5$. The results suggest that the recommended
300 level is $j = 4$, 51.38 ± 17.51 . However, the level $j = 3$ presents close results,
 45.78 ± 15.52 . Although levels 4 and 3 have good results, they are limited to
this RSI set; therefore, this procedure must be repeated in a new RSI set. The
biggest problem is when there is no GT, for example, in *in-vivo* RSIs or in
real-time applications, where it would be impractical to set the GT frame by
305 frame.

Therefore, in the proposed WA model, the j -level is selected through an
automatic denoising criterion, described in Sec. 2.3.1. The results suggest
that the proposed WA model with an automatic denoising criterion increases
the performance, 61.78 ± 17.71 concerning levels 3 and 4, 51.38 ± 17.51 and
310 45.78 ± 15.52 , respectively. We can observe that the j -levels selected by the
automatic denoising criterion are mostly $j = 4$ (64.29%). The remaining levels
are selected at $j = 3$ (21.43%) and $j = 5$ (14.29%). These results are highly
related to levels 3 and 4 without the use of the automatic denoising criterion.

3.2. Localization of blood vessels

315 The LBV process requires a synthesized image ($\dot{K}(x, y)$) as an input image.
The set of synthesized images were obtained through the method described in
Sec. 2.3. The parameters selected to perform the DWT-DP and DWT-RP
processes are described in Sec. 2.3.2. The tested RSI set is described in Sec.
2.1. In WA methodology, the LBV is a two-step process: thresholding and
320 segmentation. On the one hand, the thresholding process of the synthesized
images ($\dot{K}(x, y)$) returns performance of $52.12 \pm 18.91\%$ measured with JI. On
the other hand, the segmentation process is an improvement to the localization
of the region of interest through morphological processing was proposed in Sec.
2.4.

Table 2: Selection of the decomposition level j for the wavelet focus measured with JI.

Depth (μm)	Manual					Automatic
	1	2	3	4	5	j -level
0	51.76	57.97	72.60	78.25	55.44	88.28
200	44.71	49.01	63.31	67.02	44.79	78.27
300	43.72	50.99	64.62	64.23	38.36	77.72
400	30.88	36.57	48.36	51.95	42.18	61.96
500	25.46	28.44	39.62	48.13	27.19	52.60
600	17.75	19.46	29.26	37.95	30.13	48.68
700	15.94	17.79	28.78	36.96	30.88	47.28
900	11.70	13.07	19.70	26.56	23.60	39.41
Mean	30.24	34.16	45.78	51.38	36.57	61.78
Error	15.03	17.06	19.52	17.51	10.61	17.71

³²⁵ The results obtained after morphological processing have a mean value of $61.78 \pm 17.71\%$ of JI. There was an increase in the set with a mean value of 9.66% and a decrease in the standard deviation value of 1.2%. Although the standard deviation value did not change significantly, the mean value increases considerably, reducing the bias by negative positives. BV with $\rho \leq 400\mu m$
³³⁰ obtained a mean value of $61.78 \pm 17.71\%$ of JI above the mean of the set. In this case, the depths with the highest JI value were $0\mu m$, $200\mu m$, $300\mu m$, and $400\mu m$. BV with $\rho \geq 500\mu m$ obtained JI values below the average for the full set.

³³⁵ To compare the performance of WA model in LBV with other models reported in the *state of the art*, two LBV models were implemented: Principal Component Analysis (PCA) [22], and Morphological Approach (MA) [21].

Table 3 presents the LBV performance in three models: PCA, MA, and WA. To describe the following results, the metric used is JI, since it is desired to know the geometric similarity between the segmented image of WA model and
³⁴⁰ the GT of the RSI set. The PCA model obtained the lowest mean value. The

Table 3: Comparison of LBV performance: PCA, MA, and WA.

Depth (μm)	Precision			Sensitivity			Specificity			Jaccard Index		
	PCA	MA	WA	PCA	MA	WA	PCA	MA	WA	PCA	MA	WA
0	82.02	48.88	91.50	81.90	98.71	96.17	98.13	89.22	99.07	69.44	48.56	88.28
200	70.72	67.38	86.35	79.98	89.97	90.42	95.88	93.76	98.27	59.28	60.14	78.27
300	76.38	79.91	88.71	75.63	84.23	86.25	96.72	97.03	98.46	61.29	69.51	77.72
400	51.77	63.80	64.08	78.91	89.47	96.09	91.09	93.08	93.37	45.02	57.17	61.96
500	46.40	59.61	53.97	74.50	91.59	97.61	88.24	91.77	87.11	39.54	55.42	52.60
600	35.86	53.54	49.24	65.89	85.33	98.62	85.56	90.28	86.42	29.96	46.87	48.68
700	33.46	57.30	47.60	62.94	83.86	99.13	84.67	91.93	85.54	27.92	49.94	47.28
900	27.56	48.26	41.39	54.68	64.90	92.41	82.63	91.52	83.56	22.34	36.33	39.41
Mean	53.02	59.83	65.36	71.80	86.01	94.59	90.36	92.32	91.47	44.35	52.99	61.78
Error	20.94	10.53	20.53	9.62	9.81	4.51	5.99	2.38	6.53	17.42	9.94	17.71

JI obtained for the PCA model was $44.35 \pm 17.42\%$. The MA model obtained the lowest standard deviation value. The JI obtained for the MA model was $52.99 \pm 09.94\%$. Finally, the proposed WA model obtained the highest mean value. The proposed WA model obtained a mean value of $61.78 \pm 17.71\%$. When comparing the results obtained in this work with the previous studies, it should be noted that the proposed WA model presents an improvement in the mean value compared to the PCA and MA models. The LBV results for the RSI set are shown in Fig. 10.

3.3. Visualization of blood vessels

The process for improving the VBV from CIs with the proposed WA methodology requires as input two images: synthesized image ($K(x, y)$) and segmented image ($S(x, y)$). The synthesized images and segmented images were obtained through the method described in Sec. 2.3.2 and 2.4, respectively. The result is an improved image ($W(x, y)$).

In this work is of great interest to know how contrast values improve the VBV by attenuating noise in the region of the BV. The VBV results for the RSI set are shown in Fig. 10. The performance of the WA methodology was evaluated by two contrast improvement analyses: CNR analysis and kurtosis

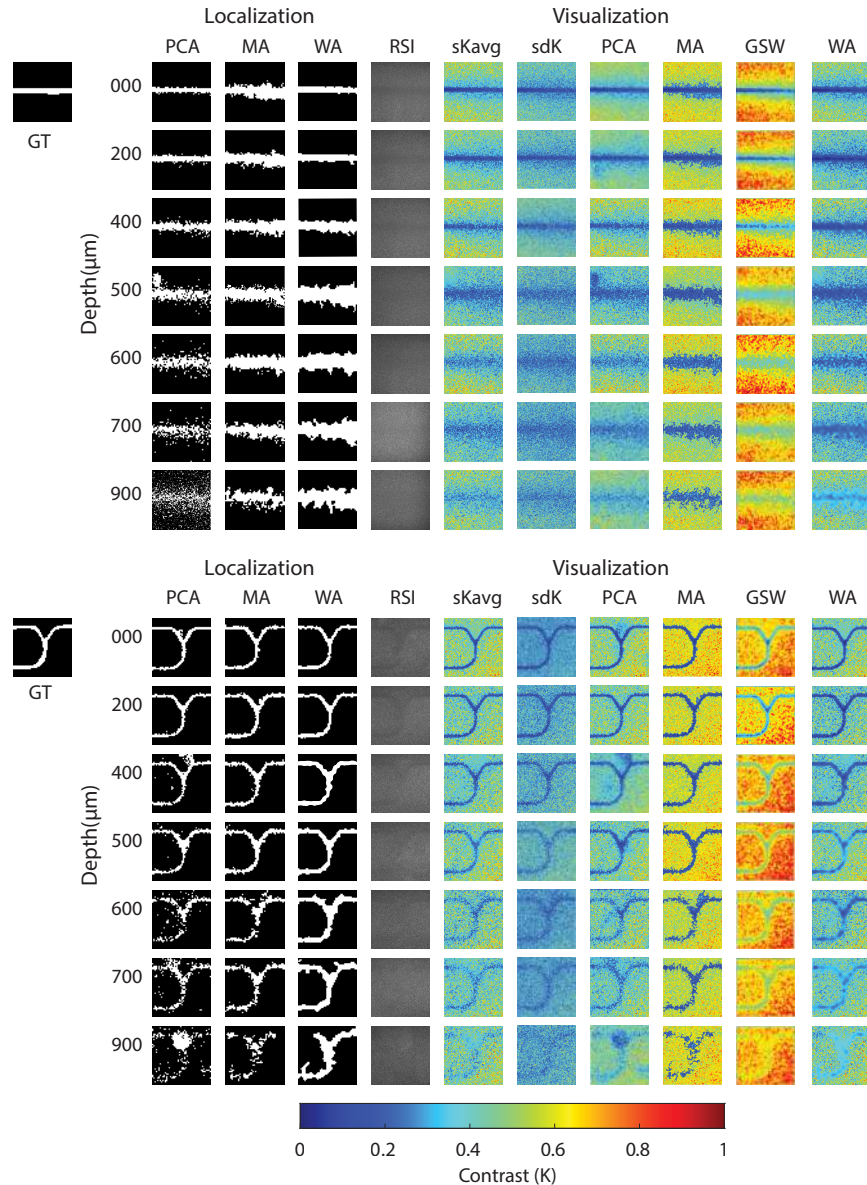


Figure 10: Results obtained from LBV and VBV for the RSI set in bifurcated and straight BV. Contrast values obtained through traditional contrast methods ($sKavg$ and sdK) and contrast improvement models (PCA, MA, GSW, WA), are normalized between 0 and 1. The ground truth (GT) consists of two classes: 1 for BV, and 0 for BT.

analysis. . On the other hand, CNR measurements are studied to know the separation between BV and BT. On the other hand, a study of the kurtosis in the contrast profiles was carried out to determine its distribution changes, explaining how contrast values improve in the BV region.

3.3.1. CNR analysis

A CNR analysis was performed to describe the contrast between BV and BT. The CNR value was determined in the improved image ($W(x, y)$) with (11) [42, 43].

$$CNR = \frac{C}{\gamma} \quad (11)$$

Where the contrast (C) is the difference of the contrast mean value between the regions (BV and BT), such as ($C = |\mu_{BV} - \mu_{BT}|$). The noise (γ) is estimated as the standard deviation of the contrast values in the region segmentation as BT. The results of the proposed WA model obtained a mean value of 2.23 ± 0.10 measured with CNR. The results suggest that noise attenuation in the BV region increases the contrast between regions (BV and BT). Noise attenuation reduces random variations inside the BV and provides a homogeneous distribution of contrast values. It is important to emphasize that despite performing a denoising process with DWT, WA model avoids combining information between regions and maintains the structure of the BV.

3.3.2. Kurtosis analysis

A kurtosis analysis was used to describe the behavior of contrast profiles. Kurtosis (κ) is a measure of the smooth or steep decay of the frequency graph of a data set to either side of the mean [44], κ is defined as:

$$\kappa(x) = \frac{1}{\sigma^4} \left[\frac{1}{n} \sum_{i=1}^n (x_i - \mu)^4 \right] \quad (12)$$

Where $x_1 \dots x_n$ are the number of observations of a quantitative variable. μ and σ are the mean and standard deviation, respectively, in one or more contrast profiles of an image [28]. There are three cases of study: the mesokurtic,

Table 4: Image quality performance to improve VBV. Traditional methods of contrast (sK , $sKavg$, sdK) and contrast improvement models (PCA, MA, GSW, WA). All experiments were conducted on a 1.8-GHz core i5 PC with 8 GB of RAM under the Matlab environment.

Depth μm	Traditional methods of contrast						Contrast improvement models							
	sK		$sKavg$		sdK		PCA		MA		GSW			
CNR	κ	CNR	κ	CNR	κ	CNR	κ	CNR	κ	CNR	κ	CNR	κ	
000	2.37	3.28	2.38	3.03	2.12	4.50	2.37	3.06	2.22	5.50	2.55	2.15	2.37	6.88
200	2.24	4.50	2.27	4.25	2.03	4.43	2.27	4.34	2.26	5.58	2.38	3.35	2.27	6.34
300	2.13	3.67	2.14	3.91	1.95	3.73	2.15	3.73	2.22	4.94	2.22	2.91	2.14	5.09
400	2.21	3.03	2.23	2.81	2.01	4.26	2.23	2.71	2.20	3.64	2.35	2.73	2.23	5.56
500	2.18	3.37	2.23	3.59	1.97	3.42	2.21	3.55	2.17	2.95	2.32	2.84	2.24	4.51
600	2.17	2.73	2.20	2.92	1.96	2.98	2.18	2.83	2.09	4.80	2.31	2.92	2.21	2.17
700	2.17	2.65	2.19	2.58	1.96	3.32	2.19	2.56	2.13	3.28	2.30	3.22	2.20	2.11
900	2.15	2.94	2.18	3.54	1.95	3.54	2.18	3.53	2.09	1.89	2.29	3.01	2.20	1.29
Mean	2.19	3.24	2.22	3.31	1.99	3.72	2.22	3.27	2.17	3.91	2.33	2.94	2.23	4.24
Error	0.11	0.75	0.10	0.70	0.08	0.70	0.09	0.71	0.07	1.92	0.15	0.39	0.10	2.12
Time	103.71		173.94		56.09		249.96		196.20		213.16		195.82	

leptokurtic, and platykurtic curves. A mesokurtic curve or standard normal distribution has a κ value ($\kappa = 3$). Leptocurtic curves have a kurtosis ($\kappa > 3$) and show an abrupt decay towards both of the mean. Finally, the platykurtic curve is that with a kurtosis ($\kappa < 3$) and presents a slow decay towards both sides of the mean.

We determined the κ value along 30 columns of each improved image ($W(x, y)$) with (12). The results obtained from the proposed WA model have a mean value of 4.24 ± 2.12 measured with κ . This is an increase in the mean value of 0.93 and standard deviation of 1.42, for the $sKavg$ method (3.31 ± 0.70). The results show a characteristic behavior of a leptokurtic curve ($\kappa > 3$). The leptokurtic curve has an abrupt decline in values around the mean, due to noise attenuation in the BV. It is important to emphasize that the performance obtained with κ indicates that the x_i data are close to the mean compared to the $sKavg$ set, and the leptokurtic curve ($\kappa > 3$) changes its distribution to platykurtic ($\kappa < 3$) as BV depth increases, which is an expected effect on CIs.

3.3.3. Performance

400 To compare the performance of quality image with CNR and κ , the results of
the proposed WA model have been compared with traditional contrast methods
and the models of contrast improvement. On the one hand, the traditional meth-
ods of contrast: spatial contrast (sK) and spatial contrast averaged ($sKavg$)
through isotropic windows are described in Sec. 2.2. A third traditional method
405 known as space-directional contrast (sdK) is introduced in [11]. sdK is an al-
ternative way of calculating contrast values with an anisotropic window. On
the other hand, Principal Component Analysis (PCA) and Morphological Ap-
proach (MA) were used in the contrast improvement models. Also, the Gaussian
Sliding Window (GSW) model was included [17]. The input image set for any
410 contrast improvement method is $sKavg$.

Table 4 presents visualization performance of BV. The results obtained by
 $sKavg$ are used as a reference in the visualization improvement. $sKavg$ presents
a CNR value (2.22 ± 0.10) and κ (3.31 ± 0.70) higher than the sK method,
supposing an improvement in the contrast values calculation. The sdK method
415 has the lowest CNR value (1.99 ± 0.09), however, it presents an improvement in
the κ value (3.72 ± 0.70). The PCA model shows a slight decrease in the CNR
value (2.22 ± 0.09) and κ (3.27 ± 0.71). The MA model shows a slight decrease
in the CNR value (2.17 ± 0.07) and an increase in the κ value (3.91 ± 1.92). The
GSW model has the highest CNR value (2.33 ± 0.15). However, the κ value
420 (2.94 ± 0.39) is the lowest of all models. WA improves the CNR of the input set
with a value of 2.23 ± 0.10 , obtaining very similar CNR values with PCA and
MA. Also, WA has the best κ value performance (4.24 ± 2.12) with the most
leptokurtic curve of all models.

4. Discussion

425 When comparing the proposed WA model with the contrast calculation
methods and contrast improvement models, it can be seen that the GSW model
presents the best CNR performance; however, it does not present consistency in

the κ values. The CNR values in GSW are due to the Gaussian filtering acting on the entire CI. This suggests two important considerations. First, the contrast values of the BV and BT have a smooth and homogeneous distribution for each area. Contrast values in BT are high, while contrast values in BV are low. This suggests that the CNR value is high, as both regions are well contrasted by avoiding regions of rapid characteristic changes in CIs. Second, the GSW filtering is non-selective and is performed equally for the BV and BT, causing information to fuse and the visualization between these two regions to decay.

This fusion effect is common in traditional contrast methods. Since they select an isotropic or anisotropic window to compute the contrast. In work [15], makes a study of the window size that should be selected to process a CI and avoid image fusion. They conclude that the size of the window for processing contrast values is related to the size of the BV. For GSW, the use of a Gaussian filter efficiently softens the noise but loses the localization of the edges of the BV with the BT. Also, filtering the contrast values could produce an over-smoothing effect. This effect is supported by kurtosis analysis, where contrast profiles are studied. κ in GSW follows a platykurtic curve. This indicates that the contrast values are far from the mean value and show a smooth decay towards both sides of the mean, a common effect in region fusion. The GSW kurtosis is even lower than $sKavg$, which has a mesokurtic curve or standard normal distribution.

On the other hand, the CNR values in WA are the result of high-frequency filtering. This suggests two important considerations. First, the region corresponding to the BT maintains the characteristic noise contrast values of the CIs, and the region of the BV has homogeneous and smoothed contrast values. Second, high-frequency filtering is selective. The shape of the selected wavelet function has a high similarity to the high-frequency noise to be removed. This allows information to be retained from the edges that separate the BV from the BT. Finally, WA kurtosis follows a leptokurtic curve. This indicates that the contrast values are closer to the mean. Besides, it shows an abrupt decay in the extreme values of the curve and indicates a lower probability of fusion between regions.

5. Conclusions

460 The VBV in RSIs is an important task to determine the vascularization inside the BT. VBV is limited due to the high scattering of static structures such as the epidermis. For this purpose, models have been developed to improve the contrast values between BV and BT. In this work, a denoising criterion was used to select an optimal level of DWT decomposition. This is to reduce the fusion
465 of BV and BT and to obtain a low-frequency representation of the CI. Then, with the low-frequency representation, a segmentation process was performed to establish the localization of the BV and BT. Finally, with the low-frequency representation and the localization of the BV, the visualization is improved by increasing the contrast in the region of the BV.

470 References

- [1] A. Cho, C. Yeon, D. Kim, E. Chung, Laser speckle contrast imaging for measuring cerebral blood flow changes caused by electrical sensory stimulation, *Journal of the Optical Society of Korea* 20 (1) (2016) 88–93.
- 475 [2] W. J. Moy, G. Ma, K. M. Kelly, B. Choi, Hemoporfirin-mediated photodynamic therapy on normal vasculature: implications for phototherapy of port-wine stain birthmarks, *Journal of clinical and translational research* 2 (3) (2016) 107.
- [3] A. Y. Neganova, D. D. Postnov, O. Sosnortseva, J. C. B. Jacobsen, Rat retinal vasomotion assessed by laser speckle imaging, *PloS one* 12 (3) (2017) e0173805.
480
- [4] P. G. Vaz, A. Humeau-Heurtier, E. Figueiras, C. Correia, J. Cardoso, Laser speckle imaging to monitor microvascular blood flow: a review, *IEEE reviews in biomedical engineering* 9 (2016) 106–120.
- 485 [5] D. D. Duncan, S. J. Kirkpatrick, Can laser speckle flowmetry be made a quantitative tool?, *JOSA A* 25 (8) (2008) 2088–2094.

- [6] J. Kim, J. Oh, B. Choi, Magnetomotive laser speckle imaging, *Journal of biomedical optics* 15 (1) (2010) 011110.
- [7] T. Son, J. Lee, B. Jung, Contrast enhancement of laser speckle contrast image in deep vasculature by reduction of tissue scattering, *Journal of the Optical Society of Korea* 17 (1) (2013) 86–90.
- [8] C. Regan, J. C. Ramirez-San-Juan, B. Choi, Photothermal laser speckle imaging, *Optics letters* 39 (17) (2014) 5006–5009.
- [9] Y. Wang, D. Wen, X. Chen, Q. Huang, M. Chen, J. Lu, P. Li, Improving the estimation of flow speed for laser speckle imaging with single exposure time, *Optics letters* 42 (1) (2017) 57–60.
- [10] A. Rege, J. Senarathna, N. Li, N. V. Thakor, Anisotropic processing of laser speckle images improves spatiotemporal resolution, *IEEE transactions on biomedical engineering* 59 (5) (2012) 1272–1280.
- [11] C. Perez-Corona, H. Peregrina-Barreto, J. Rangel-Magdaleno, R. Ramos-Garcia, J. Ramirez-San-Juan, Space-directional laser speckle contrast imaging to improve blood vessels visualization, in: 2018 IEEE International Instrumentation and Measurement Technology Conference (I2MTC), IEEE, 2018, pp. 1–5.
- [12] C. E. P. Corona, H. Peregrina-Barreto, J. C. Ramírez-San-Juan, Space-directional approach to improve blood vessel visualization and temporal resolution in laser speckle contrast imaging, *Journal of Biomedical Optics* 25 (3) (2019) 032009.
- [13] K. Basak, G. Dey, M. Mahadevappa, M. Mandal, P. K. Dutta, In vivo laser speckle imaging by adaptive contrast computation for microvasculature assessment, *Optics and Lasers in Engineering* 62 (2014) 87–94.
- [14] J. R. Velázquez-González, H. Peregrina-Barreto, J. Rangel-Magdaleno, J. C. Ramírez-San-Juan, Robust laser speckle contrast images suitable for blood vessel visualization, IEEE, 2017, pp. 1–6.

- [15] S. A. Rosales-Nunez, H. Peregrina-Barreto, J. Rangel-Magdaleno,
515 J. Ramirez-San-Juan, I. Terol-Villalobos, Automatic scale determination
for adaptive windowing in laser speckle imaging, in: 2018 IEEE Interna-
tional Instrumentation and Measurement Technology Conference (I2MTC),
IEEE, 2018, pp. 1–5.
- [16] E. B. Postnikov, M. O. Tsoy, D. E. Postnov, Matlab for laser speckle con-
520 trast analysis (lasca): a practice-based approach, in: Saratov Fall Meeting
2017: Laser Physics and Photonics XVIII; and Computational Biophysics
and Analysis of Biomedical Data IV, Vol. 10717, International Society for
Optics and Photonics, 2018, p. 1071728.
- [17] E. B. Postnikov, M. O. Tsoy, P. A. Timoshina, D. E. Postnov, Gaussian
525 sliding window for robust processing laser speckle contrast images, Interna-
tional journal for numerical methods in biomedical engineering 35 (4)
(2019) e3186.
- [18] E. Morales-Vargas, H. Peregrina-Barreto, J. Rangel-Magdaleno,
J. Ramirez-San-Juan, Estimation of blood vessels diameter by region
530 growing in laser speckle contrast imaging, in: 2019 IEEE International
Instrumentation and Measurement Technology Conference (I2MTC),
IEEE, 2019, pp. 1–5.
- [19] F. Lopez-Tiro, H. Peregrina-Barreto, J. Rangel-Magdaleno, J. Ramirez-
San-Juan, J. Ramirez-Cortes, Effect of the exposure time in laser speckle
535 imaging for improving blood vessels localization: a wavelet approach, in:
2020 IEEE International Instrumentation and Measurement Technology
Conference (I2MTC), IEEE, 2020, pp. 1–6.
- [20] E. B. Postnikov, M. O. Tsoy, M. A. Kurochkin, D. E. Postnov, A fast
method for the detection of vascular structure in images, based on the con-
540 tinuous wavelet transform with the morlet wavelet having a low central fre-
quency, in: Saratov Fall Meeting 2016: Laser Physics and Photonics XVII;

- and Computational Biophysics and Analysis of Biomedical Data III, Vol. 10337, International Society for Optics and Photonics, 2017, p. 103370X.
- [21] E. Morales-Vargas, J. Sosa-Martinez, H. Peregrina-Barreto, J. Rangel-Magdaleno, J. Ramirez-San-Juan, A morphological approach for locating blood vessels in laser contrast speckle imaging, in: 2018 IEEE International Instrumentation and Measurement Technology Conference (I2MTC), IEEE, 2018, pp. 1–6.
- [22] J. A. Arias-Cruz, R. Chiu, H. Peregrina-Barreto, R. Ramos-Garcia, T. Spezzia-Mazzocco, J. C. Ramirez-San-Juan, Visualization of in vitro deep blood vessels using principal component analysis based laser speckle imaging, *Biomedical optics express* 10 (4) (2019) 2020–2031.
- [23] P. Zakharov, A. Völker, M. Wyss, F. Haiss, N. Calcinaghi, C. Zunzunegui, A. Buck, F. Scheffold, B. Weber, Dynamic laser speckle imaging of cerebral blood flow, *Optics express* 17 (16) (2009) 13904–13917.
- [24] P. G. Vaz, A. Humeau-Heurtier, E. Figueiras, C. Correia, J. Cardoso, Effect of static scatterers in laser speckle contrast imaging: an experimental study on correlation and contrast, *Physics in Medicine & Biology* 63 (1) (2017) 015024.
- [25] X. Sang, D. Li, B. Chen, Improving imaging depth by dynamic laser speckle imaging and topical optical clearing for in vivo blood flow monitoring, *Lasers in Medical Science* 36 (2) (2021) 387–399.
- [26] F. Lopez-Tiro, H. Peregrina-Barreto, J. Rangel-Magdaleno, J. Ramirez-San-Juan, Visualization of in-vitro blood vessels in contrast images based on discrete wavelet transform decomposition, in: 2019 IEEE International Instrumentation and Measurement Technology Conference (I2MTC), IEEE, 2019, pp. 1–6.
- [27] R. B. Saager, C. Kondru, K. Au, K. Sry, F. Ayers, A. J. Durkin, Multilayer silicone phantoms for the evaluation of quantitative optical techniques in

- 570 skin imaging, in: Design and Performance Validation of Phantoms Used
in Conjunction with Optical Measurement of Tissue II, Vol. 7567, Interna-
tional Society for Optics and Photonics, 2010, p. 756706.
- [28] H. Peregrina-Barreto, E. Perez-Corona, J. Rangel-Magdaleno, R. Ramos-
Garcia, R. Chiu, J. C. Ramirez-San-Juan, Use of kurtosis for locating deep
575 blood vessels in raw speckle imaging using a homogeneity representation,
Journal of biomedical optics 22 (6) (2017) 066004.
- [29] M. Kobari, F. Gotoh, Y. Fukuuchi, K. Tanaka, N. Suzuki, D. Uematsu,
Blood flow velocity in the pial arteries of cats, with particular reference to
the vessel diameter, Journal of Cerebral Blood Flow & Metabolism 4 (1)
580 (1984) 110–114.
- [30] M. Klärhöfer, B. Csapo, C. Balassy, J. Szeles, E. Moser, High-resolution
blood flow velocity measurements in the human finger, Magnetic Resonance
in Medicine: An Official Journal of the International Society for Magnetic
Resonance in Medicine 45 (4) (2001) 716–719.
- 585 [31] M. Kimlyk, S. Umnyashkin, Image denoising using discrete wavelet trans-
form and edge information, in: 2018 IEEE Conference of Russian Young
Researchers in Electrical and Electronic Engineering (EIConRus), IEEE,
2018, pp. 1823–1825.
- [32] S. Agarwal, O. Singh, D. Nagaria, Analysis and comparison of wavelet
590 transforms for denoising mri image, Biomedical and Pharmacology Journal
10 (2) (2017) 831–836.
- [33] L. Feng, L. Lin, Image denoising methods based on wavelet transform and
threshold functions., JMPT 8 (1) (2017) 1–10.
- [34] M. J. Shensa, et al., The discrete wavelet transform: wedding the a trous
595 and mallat algorithms, IEEE Transactions on signal processing 40 (10)
(1992) 2464–2482.

- [35] I. Daubechies, Ten lectures on wavelets, Vol. 61, Siam, 1992.
- [36] L. A. Díaz, M. T. Martín, V. Vampa, Daubechies wavelet beam and plate finite elements, *Finite Elements in Analysis and Design* 45 (3) (2009) 200–209.
600
- [37] P. Navarro, C. Fernández-Isla, P. Alcover, J. Suardíaz, Defect detection in textures through the use of entropy as a means for automatically selecting the wavelet decomposition level, *Sensors* 16 (8) (2016) 1178.
- [38] Y. Han, P. Shi, An adaptive level-selecting wavelet transform for texture defect detection, *Image and Vision Computing* 25 (8) (2007) 1239–1248.
605
- [39] D.-M. Tsai, C.-H. Chiang, Automatic band selection for wavelet reconstruction in the application of defect detection, *Image and Vision Computing* 21 (5) (2003) 413–431.
- [40] S. Kotte, P. R. Kumar, S. K. Injeti, An efficient approach for optimal multilevel thresholding selection for gray scale images based on improved differential search algorithm, *Ain Shams Engineering Journal* 9 (4) (2018) 1043–1067.
610
- [41] N. Otsu, A threshold selection method from gray-level histograms, *IEEE transactions on systems, man, and cybernetics* 9 (1) (1979) 62–66.
- [42] F. Timischl, The contrast-to-noise ratio for image quality evaluation in scanning electron microscopy, *Scanning* 37 (1) (2015) 54–62.
615
- [43] M. Welvaert, Y. Rosseel, On the definition of signal-to-noise ratio and contrast-to-noise ratio for fmri data, *PloS one* 8 (11).
- [44] L. T. DeCarlo, On the meaning and use of kurtosis., *Psychological methods* 2 (3) (1997) 292.
620